J. Fluid Mech. (2005), *vol.* 539, *pp.* 387–416.
doi:10.1017/S0022112005005781 Printed in the United Kingdom

Low-Reynolds-number instabilities in three-layer flow down an inclined wall

By W. Y. JIANG[1], B. T. HELENBROOK[2], S. P. LIN[2] AND S. J. WEINSTEIN[3]

[1]Joint Center for Earth Systems Technology, University of Maryland at Baltimore County, Baltimore, MD 21250, USA

[2]Department of Mechanical and Aeronautical Engineering, Clarkson University, Potsdam, New York 13699-5725, USA

[3]Eastman Kodak Company, Rochester, New York 14652-3703, USA

(Received 12 July 2004 and in revised form 10 April 2005)

The finite wavelength instability of viscosity-stratified three-layer flow down an inclined wall is examined for small but finite Reynolds numbers. It has previously been demonstrated using linear theory that three-layer zero-Reynolds-number instabilities can have growth rates that are orders of magnitude larger than those that arise in two-layer structures. Although the layer configurations yielding large growth instabilities have been well characterized, the physical origin of the three-layer inertialess instability remains unclear. Using analytic, numerical and experimental techniques, we investigate the origin and evolution of these instabilities. Results from an energy equation derived from linear theory reveal that interfacial shear and Reynolds stresses contribute to the energy growth of the instability at finite Reynolds numbers, and that this remains true in the limit of zero Reynolds number. This is thus a rare example that demonstrates how the Reynolds stress can play an important role in flow instability, even when the Reynolds number is vanishingly small. Numerical solutions of the Navier–Stokes equations are used to simulate the nonlinear evolution of the interfacial deformation, and for small amplitudes the predicted wave shapes are in excellent agreement with those obtained from linear theory. Further comparisons between simulated interfacial deformations and linear theory reveal that the linear evolution equations are surprisingly accurate even when the interfaces are highly deformed and nonlinear effects are important. Experimental results obtained using aqueous gelatin systems exhibit large wave growth and are in agreement with both the theoretical predictions of small-amplitude behaviour and the nonlinear simulations of the large-amplitude behaviour. Quantitative agreement is confounded owing to water diffusion driven by differences in gelatin concentration between the layers in experiments. However, the qualitative agreement is sufficient to confirm that the correct mechanism for the experimental instability has been determined.

1. Introduction

The simultaneous multiple-layer flow of liquid layers down an inclined plane is a fundamental configuration often found in the manufacture of photographic products (Kistler & Schweizer 1997; Weinstein & Ruschak 2004). The inclined surfaces of a coating die distributor allow liquid layers to be stacked on top of one another in preparation for simultaneous coating on a moving substrate (a web). If the web path

after coating is inclined, gravity induces a flow with respect to the web; in the web frame, the simultaneous flow of liquid layers down a stationary inclined surface is again achieved. It is well known that the simultaneous flow of viscosity stratified layers can lead to instabilities, in the form of travelling waves, which result in undesirable thickness variations in coated products.

There is an extensive literature on instabilities arising in gravity-driven flows down inclined walls, and the reader is referred to Joseph & Renardy (1992) and Chen (1995) for relevant reviews. Initial work on flow instabilities in these configurations highlighted the importance of fluid inertia in obtaining flow instabilities as characterized by a Reynolds number, $Re = \rho U d/\mu$. Here, ρ is the fluid density, U is a characteristic velocity taken to be either the undisturbed free surface or mean velocity in the flow, d is the total film thickness, and μ is a characteristic viscosity. For example, Yih (1967) demonstrated that the two-layer viscosity-stratification instability in both plane Poiseuille and Couette flows becomes neutrally stable in the limit as $Re \to 0$. Later works, reviewed by Chen (1995), show that all two-layer interfacial flows confined within walls require inertia to destabilize liquid–liquid interfaces.

For a single-layer free-surface flow down an inclined plane, inertia is required for destabilization (Benjamin 1957; Yih 1963) as in confined configurations. However, for two-layer free-surface flows, Kao (1968), Loewenherz & Lawrence (1989) and Chen (1993) show that a travelling interfacial wave instability can arise without fluid inertia, i.e. in the $Re = 0$ approximation to the flow; this instability is thus termed inertialess. In flows having two layers or more, the number of possible travelling wave modes (excluding shear waves) is equal to the number of interfaces and free surfaces, provided that there is a jump in physical properties or interfacial tension between layers; this is due to the degrees of freedom they impart via the interface and free-surface deformability. In two-layer flows, the instability arises because of the presence of the liquid–liquid interface. The free-surface mode is found to be stable when $Re = 0$ and its character is similar to that of its single-layer counterpart (Weinstein 1990). Although the inertialess instability is primarily due to modes associated with the liquid–liquid interface, it is found that when the upper-layer free surface in a two-layer flow is removed either by replacing it with another solid wall (Renardy 1985, 1987; Chen 1995; Tilley, Davis & Bankoff 1994*a*,*b*) or by extending the upper layer to infinity (Hooper & Boyd 1983; Hooper 1985; Hooper & Grimshaw 1985), the inertialess instability does not occur.

Inertialess instability is also encountered in flows having more than two layers with a free surface (Wang, Seaborg & Lin 1978; Weinstein & Kurz 1991; Kliakhandler & Sivashinsky 1997; Weinstein & Chen 1999). Additionally, note that inertialess instabilities may now arise in such flows when they are confined by walls (Li 1969). Weinstein & Chen (1999) examine the inertialess instability in a three-layer vertical film flow in detail. They study the effect of three types of viscosity stratification with constant layer viscosities. Regardless of the viscosity configuration, the wave mode contributed by the free surface is always stable as in the two-layer case, and instabilities arise owing to the presence of the liquid–liquid interfaces. A monotonic increase of viscosity from the bottom layer to the top yields instabilities with growth rates similar to those from the two-layer instabilities having a high-viscosity upper layer as cited above. A monotonic decrease of viscosity does not yield an intertialess instability, again as in the two-layer case for a lower-viscosity top layer. Weinstein & Chen (1999) also find that when the middle layer is relatively thin, is nominally located centrally in the three-layer configuration, and is either more or less viscous than the other two layers, the disturbance growth rates are much larger than for

two-layer flows. For the case of a more viscous middle layer, there are two isolated finite bandwidths of disturbance wavelength in which the film is unstable. The largest growth occurs at very short wavelengths and the instability does not persist into the long wavelength regime. For the case of a less viscous middle layer, the large growth instabilities occur at longer, but finite, wavelengths, and can also be observed in the long-wavelength limit.

Weinstein & Chen (1999) also find that the free-surface tension can have an appreciable effect on wave growth. They also note that whenever there is a large growth-rate instability, there is a corresponding mode having the same wavelength that decays at virtually the same rate. That is, the dispersion relation between the wavelength and complex frequency yields complex conjugate modes. Weinstein & Chen suggest that this indicates there is a strong interaction between the liquid–liquid interfaces in the system (as first proposed by Li (1967) for three-layer flow between confined walls). A physical explanation for these trends has not been elucidated.

In this paper, we examine the configuration of three-layer flow down an inclined wall, and demonstrate that no satisfactory mechanism of the onset of instability can be obtained from the classical inertialess instability theories in which the acceleration of disturbances is completely neglected in the steady Stokes equations. The reason for this is given at the end of § 2. In the present work, we retain consistently the acceleration terms in both the linearized Navier–Stokes equations and the kinematic boundary condition for finite Re. We then obtain a convergent solution for the eigenvalues and the corresponding eigenfunctions. These eigen-solutions enable us to construct the energy budgets itemized in § 3. Our convergent solution for any finite Re including $Re = 0$ enables us to explain the physical mechanism of the inertialess instability in the limit of $Re = 0$. The mechanism of the onset of the instability is given in § 4. The results of our analysis and calculation show that the vestige of the instability mechanism at small finite Re persists as $Re \to 0$.

Next, to test the significance of the linear theory result, and to compare with experimental results in this paper, we carry out a direct numerical simulation based on the full Navier–Stokes equations with nonlinear boundary conditions in § 5. The method used here has been validated for many different multi-phase problems including two-layer flows (Helenbrook 2001; Helenbrook & Baker 2002; Jiang, Helenbrook & Lin 2004). Note that the weakly nonlinear evolution of three-layer flows down an inclined plane has been investigated previously at long wavelengths (Kliakhandler & Shivashinsky 1997; Kliakhandler 1999), but this work is not directly applicable here because linear stability theory predicts that short waves dominate the wave growth. Section 6 gives details of the experiments, and provides a verification of both the linear analysis and the nonlinear simulations.

2. Formulation and linear theory

Consider the simultaneous flow of three liquid layers each having the same density, ρ, under the influence of gravity, g, down a wall inclined at angle θ. The Newtonian viscosity of each layer is denoted as μ_k where $k \in [1, 3]$, the subscripts denoting the layer number where 1 is the bottom. We assume that the free surface has a constant tension σ, and that the liquid–liquid interfacial tensions are zero. The origin of an x^*–z^* coordinate system is placed at the wall, and the flow is assumed to be invariant in the y^*-direction even when disturbed. A superscript $*$ denotes a dimensional quantity, to distinguish variables from dimensionless quantities to follow. It is assumed that the dynamics of the air have a negligible effect on the flow. The

generally time-dependent location of each interface is parameterized as $z^* = \eta_k^*(x^*, t^*)$, and the x^*- and z^*-velocity components in each layer are denoted as $U_k^*(x^*, z^*, t^*)$ and $V_k^*(x^*, z^*, t^*)$, respectively, where t^* is time. The pressure in each layer is denoted as $P_k^*(x^*, y^*, t^*)$. For the undisturbed flow where all interfaces are parallel to the solid wall, the interface heights are given by $\eta_k = H_k^*$, the local velocity is in the x-direction alone denoted as $U_k^* = \overline{U}_k^*(z)$, and the pressure field is given as $P_k^* = \overline{P}_k^*(z)$.

Variables are scaled using features of the unperturbed parallel flow. The total film thickness, H_3^*, is used to scale distance. A velocity scale, U_s, is constructed from the analytical single-layer formula for the velocity at the free surface by using the bottom-layer viscosity, μ_1, the total film thickness H_3^*, and density ρ, as:

$$U_s = \frac{\rho g (H_3^*)^2 \sin\theta}{2\mu_1}. \tag{2.1a}$$

The time scales as H_3^*/U_s, and the pressure in each layer scales as ρU_s^2. These are the same scales as used by Weinstein & Chen (1999). Scaling the equations of motion, continuity, and associated boundary conditions, the following dimensionless groups arise

$$Re = \frac{\rho U_s H_3^*}{\mu_1}, \quad N_k = \frac{\mu_k}{\mu_1}, \quad H_k = \frac{H_k^*}{H_3^*}, \quad Ca = \frac{\mu_1 U_s}{\sigma}. \tag{2.1b}$$

In (2.1b), note that σ denotes the free-surface tension and $N_1 = H_3 = 1$. In what follows, the star notation ($*$) has been dropped on dependent and independent variables to indicate they are dimensionless.

The undisturbed parallel flow fields are given by

$$\overline{U}_k = -\frac{1}{N_k} z^2 + c_{k1} z + c_{k2} \quad k = 1, 2 \text{ and } 3, \quad \text{for } z \in [H_{k-1}, H_k], \tag{2.2a}$$

$$\overline{P}_k = -\frac{2\cot(\theta)}{Re} z, \tag{2.2b}$$

where

$$c_{11} = 2H_3/N_1, \tag{2.2c}$$

$$c_{12} = 0, \tag{2.2d}$$

$$c_{21} = 2H_3/N_2, \tag{2.2e}$$

$$c_{22} = \frac{H_1(H_1N_1 - H_1N_2 - 2H_3N_1 + 2H_3N_2)}{N_1N_2}, \tag{2.2f}$$

$$c_{31} = 2H_3/N_3, \tag{2.2g}$$

$$c_{32} = \big(-H_2^2N_1N_3 + H_2^2N_1N_2 + H_1^2N_1N_3 - H_1^2N_2N_3 - 2H_2H_3N_1N_2 + 2H_2H_3N_1N_3 - 2H_1H_3N_1N_3 + 2H_1H_3N_2N_3\big)/\big(N_1N_2N_3\big), \tag{2.2h}$$

In (2.2a), note that $H_0 = 0$ by definition.

To examine the instability of the basic flow given by (2.2), we perturb the basic flow

$$U_k = \overline{U}_k + u_k, \quad V_k = \overline{V}_k + v_k, \quad \eta_k = H_k + h_k, \quad P_k = \overline{P}_k + p_k \tag{2.3}$$

where u_k, v_k, h_k and p_k are dimensionless perturbation quantities. The perturbed flows (2.3) are substituted into the equations of motion, continuity and associated boundary conditions. The linearized Navier–Stokes equations are given by:

$$\boldsymbol{v}_{k,t} + \overline{\boldsymbol{U}}_k \cdot \nabla \boldsymbol{v}_k + \boldsymbol{v}_k \cdot \nabla \overline{\boldsymbol{U}}_k = -\nabla p_k + \frac{N_k}{Re} \nabla^2 \boldsymbol{v}_k \tag{2.4a}$$

$$\nabla \cdot \boldsymbol{v}_k = 0, \tag{2.4b}$$

where $\overline{\boldsymbol{U}}_k = \overline{U}_k\hat{x}$, $\boldsymbol{v}_k = u_k\hat{x} + v_k\hat{z}$, and $\hat{x}$ and $\hat{z}$ are unit vectors in the respective x- and z-directions. In (2.4*a*,*b*), the subscript k again denotes layer number, and the additional subscript t following the comma denotes partial differentiation with time; this notation will be used in what follows.

The boundary condition at the wall is the no-slip condition:

$$u_1 = v_1 = 0 \text{ at } z = 0. \tag{2.4c}$$

We first expand all variables in the interfacial boundary condition by use of the Taylor series about the unperturbed interfacial positions. Then we linearize the interfacial conditions. This allows us to apply the boundary conditions at the known unperturbed interfacial locations. Boundary conditions applied at $z = H_k$, $k = 1$ and 2 are the kinematic boundary condition

$$v_k = h_{k,t} + \overline{U}_k h_{k,x}, \tag{2.4d}$$

the velocity continuity conditions

$$v_k = v_{k+1}, \tag{2.4e}$$

$$\overline{U}_{k,z}h_k + u_k = u_{k+1} + \overline{U}_{k+1,z}h_k, \tag{2.4f}$$

the interfacial shear stress balance

$$N_k(\overline{U}_{k,zz}h_k + u_{k,z} + v_{k,x}) = N_{k+1}(\overline{U}_{k+1,zz}h_k + u_{k+1,z} + v_{k+1,x}) \tag{2.4g}$$

and the normal stress balance

$$-\overline{P}_{k,z}h_k - p_k + \frac{2N_k}{Re}v_{k,z} = -\overline{P}_{k+1,z}h_k - p_{k+1} + \frac{2N_{k+1}}{Re}v_{k+1,z}. \tag{2.4h}$$

Similarly, the free-surface boundary conditions at $z = H_3$ are the kinematic boundary condition

$$v_3 = h_{3,t} + \overline{U}_3 h_{3,x}, \tag{2.4i}$$

the shear stress balance

$$\overline{U}_{3,zz}h_3 + u_{3,z} + v_{3,x} = 0, \tag{2.4j}$$

and the normal stress boundary condition

$$-\overline{P}_{3,z}h_3 - p_3 + \frac{2N_3}{Re}v_{3,z} - We_3^{-1}h_{3,xx} = 0, \tag{2.4k}$$

where $We_3 = Ca\ Re$ is a Weber number.

To solve the linearized system (2.4), a streamfunction $\psi_k U_s H_3^*$ is introduced in each layer that satisfies $u_k = \partial\psi_k/\partial y$ $v_k = -\partial\psi_k/\partial x$. Thus, the continuity equation (2.4*b*) is implicitly satisfied and the explicit appearance of both velocity components is eliminated. The transformed equations admit superimposed travelling waves having the Fourier components:

$$\psi_k = \varphi_k(z)\,\mathrm{e}^{\mathrm{i}(\alpha x - \omega t)}, \tag{2.5a}$$

$$h_k = A_k\,\mathrm{e}^{\mathrm{i}(\alpha x - \omega t)}, \tag{2.5b}$$

where it is understood that only the real part is physically significant. In (2.5), $\varphi_k(z)$ is a flow eigenfunction, A_k is the possibly complex amplitude of the interfacial or free-surface movement, and $\mathrm{i} = (-1)^{1/2}$; additionally, α is a purely real dimensionless wavenumber that is related to the dimensionless wavelength λ as $\alpha = 2\pi/\lambda$, and $\omega = \omega_R + \mathrm{i}\omega_I$ is the complex dimensionless frequency defined in terms of real quantities

ω_R and ω_I. The dimensional counterpart of wavelength and frequency are defined as $H_3^*\lambda$ and $\omega U_s/H_3^*$, respectively. Substituting the form (2.5) into the kinematic constraints (2.4*a*) and (2.4*d*) yields a relation between A_k and $\varphi_k(H_k)$ (i.e. the value of $\varphi_k(z)$ at each unperturbed interface). This allows us to reduce the linearized system (2.4) into a generalized eigenvalue problem to solve for the complex relation $\omega = \omega(\alpha)$ and the eigenfunctions $\varphi_k(z)$. With small notational differences, the resulting system of equations, which constitutes a linear eigenvalue problem, is identical to that solved by Weinstein & Chen (1999) if $Re = 0$ is assumed. In the current work, however, we preserve the appearance of inertia so we can examine the limiting process for finite, but small, Re as $Re \to 0$.

In the presentation of data that follows, we find it useful to write explicitly the equation for the interface shape in travelling-wave form by employing (2.5*b*) and complex polar form as:

$$A_k = a_k \, \mathrm{e}^{\mathrm{i}\gamma_k}, \tag{2.6a}$$

where a_k and γ_k are the magnitude and phase. We can then write the real interface solution as:

$$h_k = a_k \exp(\omega_I t)\cos[\alpha(x - ct) + \gamma_k] \quad \text{for } k \in [1, 3], \tag{2.6b}$$

where c is the wave speed (purely real) given by:

$$c = \frac{\omega_R}{\alpha}. \tag{2.6c}$$

In the inertialess instability theory of Weinstein & Chen (1999), Re is put to zero *a priori* in (2.4*a*), and thus the inertia term drops out. This asymptotic procedure, however, restricts the range of frequencies and wavenumbers that may be examined as follows. When (2.5) is substituted into (2.4*a*), the time and space derivatives bring out, respectively, ω and α to the coefficients of the inertia term. Consequently, the local and convective acceleration terms are, respectively, of orders $Re\omega$ and $Re\alpha$. This indicates that large wavenumber and frequency disturbances satisfying $(\omega, \alpha) = 0(Re^{-1})$ are excluded when $Re = 0$ is assumed. Thus, if the disturbance is to be constructed with all possible frequency and wavenumber by use of Fourier superposition of all normal modes, then the acceleration term must be retained even in the limit of $Re = 0$. Thus, to assure that instabilities are examined in the most general way, the inertia term must be retained in the governing equation as well as in the kinematic boundary condition. In the present work, convergent series solutions which are uniformly valid for all ω and α and finite Re, including $Re = 0$, are obtained. The solutions allow us to calculate the energy budget delineated in the next section, and to evaluate the time rate of energy growth in the bulk of the flow. The uniformly convergent solutions enable us to explain unambiguously the physical significance of inertialess instability as the limiting case of $Re \to 0$. In passing, we point out that even if the inertialess instability solution is considered to be the lowest-order regular perturbation solution valid in the frequency and wavenumber ranges mentioned above (i.e. $Re\omega \ll 1$, $Re\alpha \ll 1$), the time rate of energy growth of disturbances in the bulk flow can be assessed only in the next-order solution that incorporates inertial terms (but again, is restricted to the same frequency and wavenumber ranges).

3. Derivation of energy equation

The details of the derivation of the energy equation for a two-layered film flow are given by Jiang *et al.* (2004). The derivation for the present three-layer case is similar.

Therefore, only the outline of the derivation is given here. To obtain the energy equation, we form the dot product of (2.4*a*) with $\boldsymbol{v}_k$, and integrate over the control volume per unit width consisting of the coating thickness $H_3(=1)$ and one dimensionless wavelength. We then integrate over one dimensionless period of the disturbance $2\pi/\omega_R$, convert the volume integrals to surface integrals by use of the divergence theorem whenever applicable, and apply boundary conditions (2.4*c–k*) to the resulting surface integrals. The resulting energy budget reads:

$$\mathrm{KIN} - (\mathrm{RE}_1 + \mathrm{RE}_2 + \mathrm{RE}_3) = \mathrm{DI}_1 + \mathrm{DI}_2 + \mathrm{DI}_3 + \mathrm{SH}_1 + \mathrm{SH}_2 + \mathrm{SH}_3 + \mathrm{SUF} + \mathrm{PRF}, \tag{3.1a}$$

where

$$\mathrm{KIN} = \sum_{k=1}^{3} \frac{\omega_R}{4\pi\lambda} \int_0^{2\pi/\omega_R} \frac{\mathrm{d}}{\mathrm{d}t} \int_{H_{k-1}}^{H_k} \int_0^{\lambda} \left(u_k^2 + v_k^2\right) \mathrm{d}x\, \mathrm{d}z\, \mathrm{d}t, \tag{3.1b}$$

$$\mathrm{RE}_k = -\frac{\omega_R}{2\pi\lambda} \int_0^{2\pi/\omega_R} \int_{H_{k-1}}^{H_k} \int_0^{\lambda} u_k v_k \overline{U}_{k,z}\, \mathrm{d}x\, \mathrm{d}z\, \mathrm{d}t, \tag{3.1c}$$

$$\mathrm{DI}_k = -\frac{N_k \omega_R}{2\pi\lambda Re} \int_0^{2\pi/\omega_R} \int_{H_{k-1}}^{H_k} \int_0^{\lambda} [2(u_{k,x})^2 + (u_{k,z} + v_{k,x})^2 + 2(v_{k,z})^2]\, \mathrm{d}x\, \mathrm{d}z\, \mathrm{d}t, \tag{3.1d}$$

$$\mathrm{SH}_k = \frac{N_k \omega_R}{2\pi\lambda Re} \int_0^{2\pi/\omega_R} \int_0^{\lambda} [(u_k - u_{k+1})(u_{k,z} + v_{k,x})]_{z=H_k}\, \mathrm{d}x\, \mathrm{d}t, \tag{3.1e}$$

$$\mathrm{SUF} = \frac{\omega_R}{2\pi\lambda CaRe} \int_0^{2\pi/\omega_R} \int_0^{\lambda} (v_3 h_{3,xx})_{z=H_3}\, \mathrm{d}x\, \mathrm{d}t, \tag{3.1f}$$

$$\mathrm{PRF} = \frac{\omega_R}{2\pi\lambda} \int_0^{2\pi/\omega_R} \int_0^{\lambda} (v_3 h_3 \overline{P}_{3,z})_{z=H_3}\, \mathrm{d}x\, \mathrm{d}t. \tag{3.1g}$$

KIN represents the change of kinetic energy averaged over one wavelength and one period of the disturbance fluctuation. It is positive, negative or zero, depending on whether the flow is unstable, stable or neutrally stable. The other terms may be positive or negative, depending on whether they do the work on, or drain the energy from, the bulk of the fluid. RE_1, RE_2 and RE_3 represent, respectively, the Reynolds stress work rate in the lower, middle and upper layers; DI_1, DI_2 and DI_3 represent the respective energy dissipation in layers 1, 2 and 3; SH_1 is the rate of work done by the shear stress at the interface $z = H_1$ owing to the discontinuity in the disturbance velocity, so that the velocity at the deformed interface can be continuous; similarly, SH_2 is the rate of work at the interface $z = H_2$; SH_3 is the shear stress work rate required at the free surface $z = H_3$, so that the deformed free surface can be shear free. In the formula for SH_3, u_4 should be replaced by zero. SUF is the rate of surface tension work on the three-layer film flow; and the last term in (3.1*a*) represents the pressure work on the top layer. Note that $\overline{P}_3$ in PRF is proportional to $1/Re$ as shown in (2.2*a*), and is zero for a vertical film flow.

In order to evaluate the energy budget, we must know the perturbation eigenfunctions (v_k, p_k, h_k). These are obtained from the solution to the system (2.4) using the

forms of the perturbed velocities and interface locations (2.5). The required eigenvalues and eigenfunctions have been obtained here by use of the Chebyshev collocation method for finite Re and finite wavelength λ. The eigenvectors are obtained by use of subroutine EIG in Matlab. Sufficiently large numbers of Chebyshev collocation points are retained to ensure the required numerical accuracy. The obtained eigenvalues are compared with the results of Weinstein & Chen (1999) and Weinstein & Kurz (1991) in the ranges of wave frequency and wavenumbers in which the inertia terms may be neglected. It is found that results are in excellent agreement.

The obtained eigenfunctions are used to evaluate the real physical variables appearing in each integrand in (3.1). Each integrand is evaluated by use of QUADL in Matlab. Note that the integration over t and x can be carried out by hand. The sum of all integrals on the right-hand side of (3.1a) must be equal to the left-hand side of (3.1a) which is evaluated independently. This provides an additional check for numerical accuracy. For all of the finite-Reynolds-number numerical results reported, the left-hand side and the right-hand side agree at least up to three significant digits. In the zero-Reynolds-number case, a different procedure is used which will be discussed later. It should be pointed out that the eigenfunctions are obtained here with a convergent series for any finite Re including the limiting case of $Re \to 0$. In addition to providing the integrands in (3.1), the obtained eigenvectors allow us to examine the evolution of stable and unstable interfacial waves within the confines of linear theory. This allows us to compare results with those from the simulation and experimental results to follow.

4. Mechanism of the three-layer inertialess instability

Weinstein & Chen (1999) found that among four typical viscosity stratifications, the configuration with a thin middle layer having either the smallest or largest viscosity gives the most prominent instability. We will examine cases similar to those investigated in Weinstein & Chen – a thin less viscous middle layer and a thin more viscous middle layer. For both cases, we fix θ at $\pi/2$, and keep the top- and bottom-layer viscosities the same. Only the middle-layer viscosity is varied. In such configurations, the high growth unstable mode occurs in a pair with a mode having the same wavelength, but damps at almost the same rate. That is, the normal modes are characterized by almost exactly complex conjugated eigenvalues, $\omega(\alpha)$ in (2.5). In what follows, we examine the unstable interfacial mode.

The eigenvector describing the unstable mode is determined only up to an arbitrary multiplication factor. Only the sign and relative magnitude of each term in the energy budget (3.1a) is of importance. To give the absolute magnitude of KIN some physical significance, we normalize the eigenvectors such that the magnitude of KIN is equal to ω_I, the unstable growth rate. The numerical values of KIN and some of the energy budget items on the right-hand side of (3.1a) are given in table 1 and are plotted in figure 1 for the case of a less-viscous middle layer ($Re = 0.1$, $N_2 = 0.2$, $H_1 = 0.475$, $H_2 = 0.525$, and $Ca = 0.001$). The values are chosen to coincide with those of figure 3 of Weinstein & Chen except at finite Reynolds number. (There are typographical errors in the value of Ca in figures 2–14 of Weinstein & Chen (1999), $Ca = 1000$ should read $Ca^{-1} = 1000$.) The first column gives the wavelength λ; the wavelength range chosen corresponds to the high growth unstable range identified by Weinstein & Chen. The largest magnitude terms are the dissipation terms, DI_1, DI_2 and DI_3, and interfacial shear terms, SH_1 and SH_2; these are of the same order of magnitude. The power delivered to each layer through

λ	KIN	DI_1	DI_2	DI_3	SH_1	SH_2	SH_3	SUF
1.84	5.65×10^{-2}	-3.84608×10^{2}	-8.24207×10^{2}	-3.84575×10^{2}	1.03165×10^{3}	5.61548×10^{2}	-9.480×10^{-4}	-4.598×10^{-3}
2.06	1.42×10^{-1}	-1.48236×10^{2}	-3.08448×10^{2}	-1.43225×10^{2}	4.02127×10^{2}	1.97595×10^{2}	-1.530×10^{-3}	-5.330×10^{-3}
2.31	1.78×10^{-1}	-8.94165×10^{1}	-1.76046×10^{2}	-8.24289×10^{1}	2.42198×10^{2}	1.05550×10^{2}	-1.909×10^{-3}	-4.857×10^{-3}
2.59	1.96×10^{-1}	-6.38099×10^{1}	-1.16332×10^{2}	-5.54524×10^{1}	1.70843×10^{2}	6.46368×10^{1}	-2.435×10^{-3}	-4.656×10^{-3}
2.99	2.04×10^{-1}	-4.64112×10^{1}	-7.49340×10^{1}	-3.68373×10^{1}	1.21359×10^{2}	3.67361×10^{1}	-3.334×10^{-3}	-4.643×10^{-3}
3.36	2.02×10^{-1}	-3.80711×10^{1}	-5.49019×10^{1}	-2.77574×10^{1}	9.73140×10^{1}	2.33465×10^{1}	-4.338×10^{-3}	-4.855×10^{-3}
3.66	1.98×10^{-1}	-3.36347×10^{1}	-4.42866×10^{1}	-2.28726×10^{1}	8.44783×10^{1}	1.62570×10^{1}	-5.309×10^{-3}	-5.122×10^{-3}
4.11	1.90×10^{-1}	-2.93074×10^{1}	-3.39446×10^{1}	-1.80222×10^{1}	7.19384×10^{1}	9.29006	-7.029×10^{-3}	-5.742×10^{-3}
4.48	1.82×10^{-1}	-2.67657×10^{1}	-2.80694×10^{1}	-1.51935×10^{1}	6.46437×10^{1}	5.34818	-8.688×10^{-3}	-6.403×10^{-3}
5.64	1.57×10^{-1}	-2.21428×10^{1}	-1.77127×10^{1}	-1.00103×10^{1}	5.15354×10^{1}	-1.68229	-1.564×10^{-2}	-9.426×10^{-3}
7.10	1.32×10^{-1}	-1.95076×10^{1}	-1.19787×10^{1}	-6.97409	4.41619×10^{1}	-5.68518	-2.908×10^{-2}	-1.569×10^{-2}
8.93	1.09×10^{-1}	-1.77653×10^{1}	-8.55834	-5.07307	3.94264×10^{1}	-7.96824	-5.493×10^{-2}	-2.811×10^{-2}
1.73×10^{1}	5.80×10^{-2}	-1.56896×10^{1}	-4.64381	-2.84365	3.35471×10^{1}	-9.81353	-3.840×10^{-1}	-1.823×10^{-1}
3.17×10^{1}	2.93×10^{-2}	-1.43415×10^{1}	-3.95198	-3.43203	3.07631×10^{1}	-5.76904	-2.422	-8.507×10^{-1}
5.32×10^{1}	1.33×10^{-2}	-1.11483×10^{1}	-5.00865	-8.47915	3.75791×10^{1}	-6.81704	-5.365	-7.634×10^{-1}
9.46×10^{1}	6.80×10^{-3}	-9.54203	-5.02363	-9.46683	4.41036×10^{1}	-1.54772×10^{1}	-4.448	-1.481×10^{-1}
1.78×10^{2}	3.61×10^{-3}	-9.23940	-4.87299	-9.24539	4.45812×10^{1}	-1.71757×10^{1}	-4.027	-2.177×10^{-2}
3.26×10^{2}	1.97×10^{-3}	-9.19425	-4.84240	-9.19693	4.45635×10^{1}	-1.73620×10^{1}	-3.965	-3.543×10^{-3}

TABLE 1. Partial energy budget for disturbances at $Re = 0.1$, $N_1 = N_3 = 1$, $N_2 = 0.2$, $H_1 = 0.475$, $H_2 = 0.525$, $H_3 = 1$, $We_1 = We_2 = 0$, $Ca = 0.001$ and $\theta = \pi/2$.

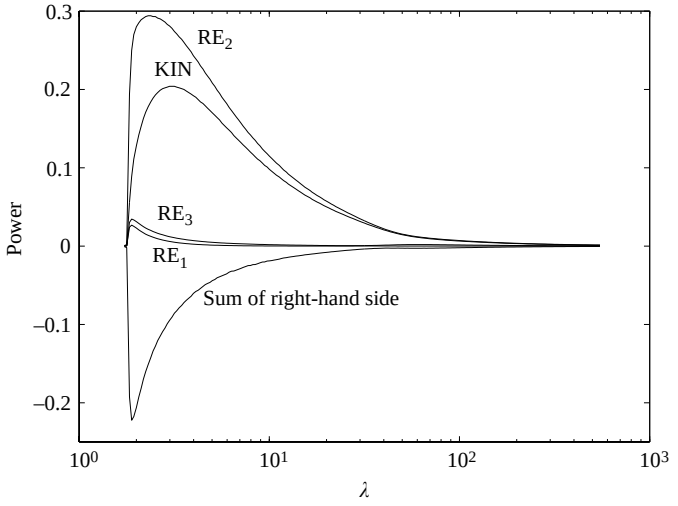

FIGURE 1. The dependence of the power contributed from various terms in the energy budget on the wavelength, λ, for a low-viscosity middle-layer configuration at low Reynolds numbers. $Re = 0.1$, $N_1 = N_3 = 1$, $N_2 = 0.2$, $H_1 = 0.475$, $H_2 = 0.525$, $H_3 = 1$, $Ca = 0.001$ and $\theta = \pi/2$.

interfacial shear is always positive, and the viscous dissipation is always negative, as they should be. Thus, the interfacial shear is always destabilizing and viscous dissipation is always stabilizing. The work rate terms SH_3 and SUF at the free surface are negative. The magnitude of the sum of DI_1, DI_2, DI_3 and SUF is larger than that of the sum of SH_1 and SH_2. Thus, the power by interface shear work is drained mainly by the viscous dissipation and weakly by the free-surface tension work and shear work.

Figure 1 shows that the sum of the right-hand-side terms is negative which implies that the Reynolds stresses must be included to have positive energy growth. RE_2 is greater than KIN, thus the energy transferred by the thin less-viscous layer is enough to cause the kinetic energy growth shown in the figure. Although this is true, we emphasize that the interfacial shear work terms give 3 orders of magnitude more energy production for this case. The Reynolds stresses provide just enough energy to make the entire sum positive. To verify whether the above situation continues in the limit of zero Reynolds number, we obtain results for $Re = 0.05$ and $Re = 0.01$ also. For these cases, the relative magnitudes of KIN, RE_1, RE_2 and RE_3 are almost identical to those in figure 1. We note that for the Re in this range, the left-hand and right-hand sides of the energy budget agree to more than 8 significant digits.

We cannot examine the limiting case of $Re = 0$ directly because each term on the right-hand side of the energy budget (3.1*a*) is divided by Re. However, if we multiply the right-hand side through by Re and evaluate each term in (3.1*a*), we find that the right-hand side consists of large-magnitude dissipation and shear work terms (such as in table 1) whose difference is exceedingly small as $Re \to 0$. Thus, the right-hand side actually has an indeterminate form of $0/0$ in the limit of $Re = 0$, and L'Hôpital's rule applies. Numerically, we cannot retain accuracy in this limiting process. However, our results for finite but increasingly small Re in the range of numerical accuracy demonstrates that the sum of these terms remains finite. On the other hand, the left-hand side of (3.1*a*), however, always retains numerical accuracy in the limit, as no indeterminate form arises. Therefore, we can use the sum of the left-hand side terms

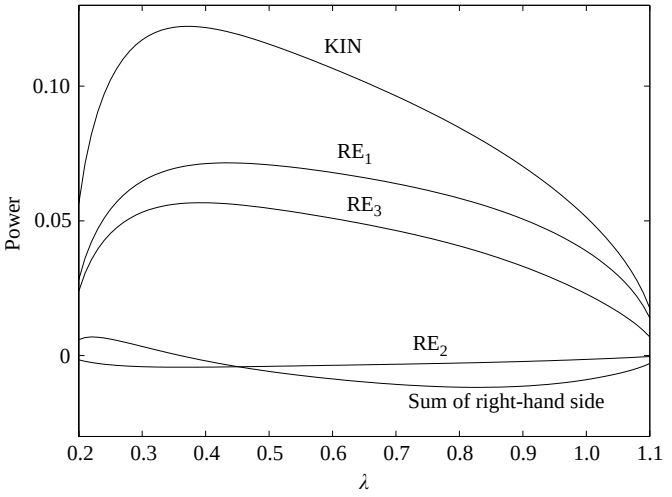

FIGURE 2. The dependence of the power contributed from various terms in the energy budget on the wavelength, λ, for a low-viscosity middle-layer configuration at low Reynolds numbers. $Re = 0.1$, $N_1 = N_3 = 1$, $N_2 = 5$, $H_1 = 0.475$, $H_2 = 0.525$, $H_3 = 1$, $Ca = 0.001$ and $\theta = \pi/2$.

to evaluate the sum of the right-hand side terms, since both must always be equal. If we then make a plot similar to figure 1 but for zero Reynolds number, we find that the results are indistinguishable from those shown in figure 1. This confirms that the Reynolds stresses must be included to have positive energy growth in the limit of $Re \to 0$. The Reynolds stresses remain positive in the limit of $Re \to 0$ while the sum of the shear work and dissipation terms remains negative. Usually, the Reynolds stress contribution to hydrodynamics instability and its role in turbulence generation is associated with large-Reynolds-number flows. We have offered here a rare example of the crucial role of the Reynolds stress in the low-Reynolds-number instability of stratified flows.

Figure 2 shows the case when the middle layer is more viscous. The flow parameters are the same as those of figure 1 except $N_2 = 5$. Note that there is a wavelength regime shown in figure 2, i.e. $0.2 \leqslant \lambda \leqslant 0.36$, for which the sum of the right-hand side is positive and thus contributes to wave growth; this is qualitatively different from the case of a less viscous middle layer, as shown in figure 1, where the right-hand side is always negative. Nevertheless, over the whole wavelength range, figure 2 shows that RE_1 and RE_3 are the main contributors to KIN, and thus it is the Reynolds stress in the lower-viscosity layers that is primarily responsible for the energy growth of the flow. If we recalculate figure 2 at $Re = 0$, we again find that the situation remains the same.

The Reynolds stress can also explain the effects of the free-surface tension and the thickness ratios on the inertialess instability. Weinstein & Chen in their figure 15 showed that the free-surface tension has significant effects on the instability of the flow, especially in the range $0.02 < Ca < 2.5$. Figures 3 and 4 show KIN, RE_1, RE_2 and RE_3 for the maximum growth rate of all wavenumbers as the capillary number changes. The flow parameters in figure 3 are the same as those in figure 15 of Weinstein & Chen and $N_2 = 0.2$. From figure 3, we can see that RE_2 is always greater than KIN and is much greater than RE_1 and RE_3. Thus, the energy transferred by Reynolds stress in the middle layer is crucial for the instability, as found in figure 1. It is the variation of RE_2 that causes the steep slope of the growth rate in the range

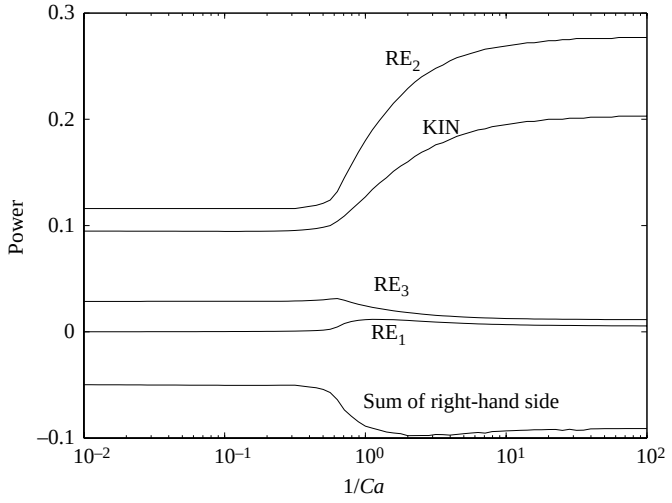

FIGURE 3. The dependence of the power contributed from various terms in the energy budget on the inverse capillary number, $1/Ca$, for a low-viscosity middle-layer configuration at $Re = 0$. Results are given for the maximum growth rate of all wavelengths for a given capillary number. $N_1 = N_3 = 1$, $N_2 = 0.2$, $H_1 = 0.475$, $H_2 = 0.525$, $H_3 = 1$ and $\theta = \pi/2$.

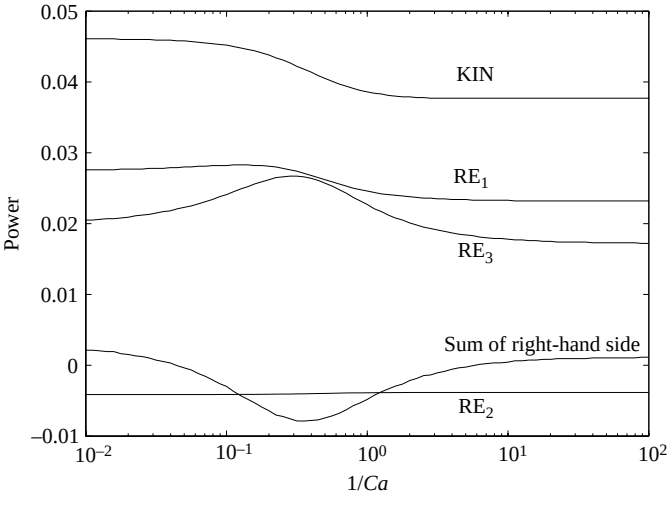

FIGURE 4. The dependence of the power contributed from various terms in the energy budget on the inverse capillary number, $1/Ca$, for a high-viscosity middle-layer configuration at $Re = 0$. Results are given for the maximum growth rate of all wavelengths against the inverse capillary number. $N_1 = N_3 = 1$, $N_2 = 2.5$, $H_1 = 0.475$, $H_2 = 0.525$, $H_3 = 1$, and $\theta = \pi/2$.

$0.02 < Ca < 2.5$. Meanwhile, the sum of the dissipation, shear and other work terms remains negative. Therefore, the capillary number affects the instability by promoting greater energy transfer in the middle layer through the Reynolds stress. The effect of surface tension on a flow with a more viscous middle layer is shown in figure 4. We choose the same flow parameters as those in figure 16 of Weinstein & Chen and $N_2 = 2.5$. In contrast to the case of a less viscous middle layer, RE_1 and RE_3 are now crucial for the instability of the flow, as also seen in figure 2. The effect of the surface tension on the Reynolds stress solidifies the arguments of Loewenherz & Lawrence

(1989) that the eigenfunctions are affected by the whole flow field and thus have a global character, even while it is the local presence of the liquid interfaces that allows for the existence of unstable modes.

The above results show that the Reynolds stress in the less viscous layers, no matter how small, is required to induce instability in the limiting case of $Re \to 0$. Other data, not shown here, verifies that this conclusion is generally valid for cases in which relative layer thicknesses and positions are varied, such as shown in figures 6, 8, 13 and 14 of Weinstein & Chen (1999). It should be pointed out that our conclusions are established through the use of convergent series solutions for eigenvectors. This allows us to establish firmly that the inertialess instability predicted by previous workers on the basis of the Stokes equation is physically significant.

5. Nonlinear simulations

In this section, we present nonlinear simulations of three-layer flows and compare the results to the linear analysis. The method used to perform the simulations is an *hp*(h = mesh resolution, p = polynomial order)-finite-element method developed for Navier–Stokes simulations of incompressible multi-fluid flows. It uses arbitrary-Lagrangian–Eulerian (ALE) mesh movement to follow the position of the free surface and interfaces. At these surfaces, the fully nonlinear kinematic and jump conditions are enforced. The combination of *hp* finite elements with ALE mesh movement allows us to obtain a high order of spatial accuracy for this problem. For the simulations presented here, a fourth-order polynomial basis is used which gives fifth-order spatial accuracy. In time, a 4-step diagonally-implicit Runge–Kutta (DIRK) formulation is used (Williams *et al.* 2002), which gives third-order temporal accuracy. We also use a mesh adaptation algorithm to resolve fine-scale features. The *hp* finite-element method is described by Helenbrook (2001) and the adaptation algorithm is described in Helenbrook & Baker (2002). We examine two cases corresponding to those examined in the energy budget analysis. The only change is that, to match the experiment (§ 6), we set the Reynolds number to 0.01.

5.1. *Less viscous middle layer*

The first case has a less viscous middle layer and is given by $Re = 0.01$, $N_2 = 0.2$, $H_1 = 0.475$, $H_2 = 0.525$ and $Ca = 0.001$. This is identical to the conditions of table 1 except the Reynolds number is a factor of 10 smaller in the simulation. We use a periodic domain in the direction parallel to the flow. Periodic boundary conditions are compatible with the base solution and the perturbation solutions of the linearized analysis. For these conditions, the most-unstable wavelength is approximately 3 times the depth, therefore we set the non-dimensional domain length to 3 in order to examine the most unstable mode. The initial element mesh and domain are shown in figure 5. The resolution of the simulation is four times that of the element mesh because on each element there is a fourth-order polynomial space. A non-dimensional time step of 0.0625 is used for the calculation. We have analysed the DIRK scheme (ignoring the spatial discretization error), and at this time step the growth rate of the unstable mode will be predicted with less than 1% error.

For initial conditions, we assume the flow is at the base state given by (2.2). The interface location h_1 is then given a sinusoidal perturbation while h_2 and the free-surface are left unperturbed. The initial perturbation is a sine wave of wavelength 3 and amplitude of 0.001. Figure 6 shows the profile of the middle layer at time intervals corresponding to one period of propagation. The free-surface position is not

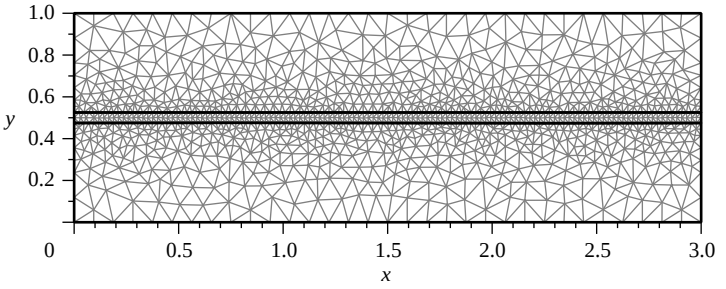

FIGURE 5. Initial element mesh for case IA simulation.

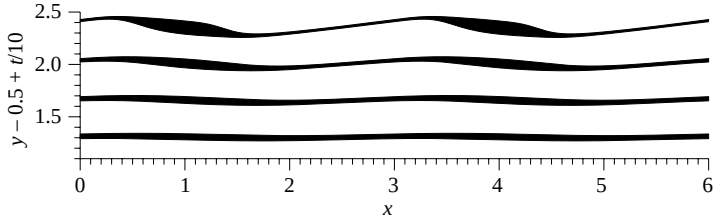

FIGURE 6. Interfacial positions for various times for a low-viscosity middle-layer configuration corresponding to $Re = 0.01$, $N_1 = N_3 = 1$, $N_2 = 0.2$, $H_1 = 0.475$, $H_2 = 0.525$, $H_3 = 1$, $Ca = 0.001$ and $\theta = \pi/2$.

shown because it remains nearly perfectly flat during the simulation. For visualization purposes, the position of the middle layer is shifted upward with time according the formula, $y = y - 0.5 + t/10$. $t = 0$ then corresponds to having the middle layer centred at $y = 0$ on the figure, and the middle layer shifts up 0.35 each period. We show two wavelengths of the disturbance to facilitate comparison with the experimental layer cross-sections shown in the § 6.

The first profile shown is after approximately four periods of propagation. At this time, nonlinear effects are not significant and the interfacial shapes are still fairly sinusoidal. The upper sinusoid is shifted slightly to the downstream direction (to the right) which leads to a thicker downward sloped region. As the amplitude of the perturbation grows, nonlinear effects play an increasingly important role. The last profile corresponds to a time at the end of the simulation. The interface shapes are no longer sinusoidal, and we have large beads of fluid separated by thin strands. This behaviour is also seen in the experimental results, as we will see in § 6.

An intriguing aspect of the nonlinear evolution is how well it is predicted by linear analysis. If we normalize the eigensolution of the unstable mode such that $a_1 = 0.001$ and $\gamma_1 = 0$ in (2.6*b*), then $a_2 = 0.974 a_1$ and $\gamma_2 = -0.62$. Figure 7 shows the interface and free-surface shapes predicted by linear theory for these parameters. The amplitude grows exponentially and translates in time according to (2.6*b*) with $\omega_I = 0.204$ and $c = 0.850$. Note that the interface evolution in figure 7 looks remarkably similar to that in figure 6. At the last time shown, the linear theory predicts that the upper and lower interfaces intersect. However, the linear theory predicts the profiles well, up to the point at which the position of the middle layer rises and falls with an amplitude that is larger than its thickness.

Furthermore, figure 8 shows the x position of the extrema of the middle layer, namely the minimum of h_1 and the maximum of h_2, as a function of time. To remove

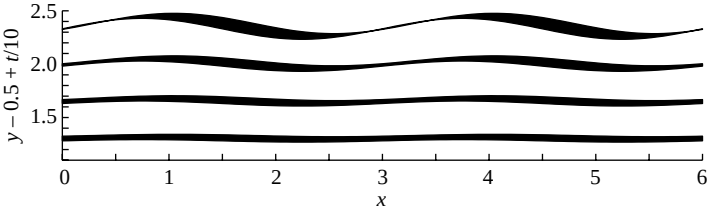

FIGURE 7. Shapes of the interfaces for the most unstable wave predicted from linear theory at the same conditions of figure 6. Parameters for the linear solution are $a_1 = 0.001$, $\gamma_1 = 0$, $a_2 = 0.973a_1$, $\gamma_2 = -0.62$, $\omega_I = 0.204$, and $c = 0.850$.

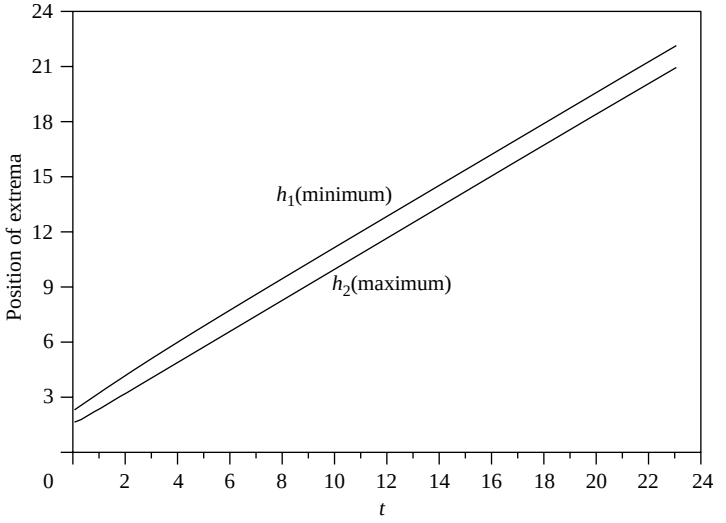

FIGURE 8. Position of minimum of h_1 and maximum of h_2 as a function of time.

the jumps that occur because of the periodic boundaries, each time the extrema passes through the periodic boundary, we add a domain length to its position. From this plot, we see that the position curves are almost perfectly linear, implying that the propagation velocity of the disturbance, c, is a constant. The last time shown on the figure corresponds to the last condition shown in figure 6. On figure 8, a propagation period corresponds to a vertical shift of distance 3 (the wavelength). There is a very slight deviation from linear for the first period of propagation. This deviation is because of the initial conditions. The initial conditions are a linear combination of several modes, therefore one unique speed for the disturbance cannot be identified. As the unstable mode grows and the other modes decay, the behaviour is dominated by the unstable mode. If we fit lines to the data excluding the first period, we find propagation speeds equal to $c = 0.846$ for h_1 and $c = 0.843$ for h_2 compared to the prediction of $c = 0.850$ from the linear analysis from (2.6*b*). Thus, the linear analysis provides a very good prediction of the propagation velocity. This prediction remains accurate even to the nonlinear conditions shown in figure 6.

The phase shift between the upper and lower interface shapes, $\gamma_2 - \gamma_1$ in (2.6*b*) is shown as a function of time in figure 9. Examining the figure, we find that after an initial transient period, the phase shift varies in the range of -0.65 to -0.70 radians. As discussed above, the linear analysis predicts a value of -0.62 so there is again

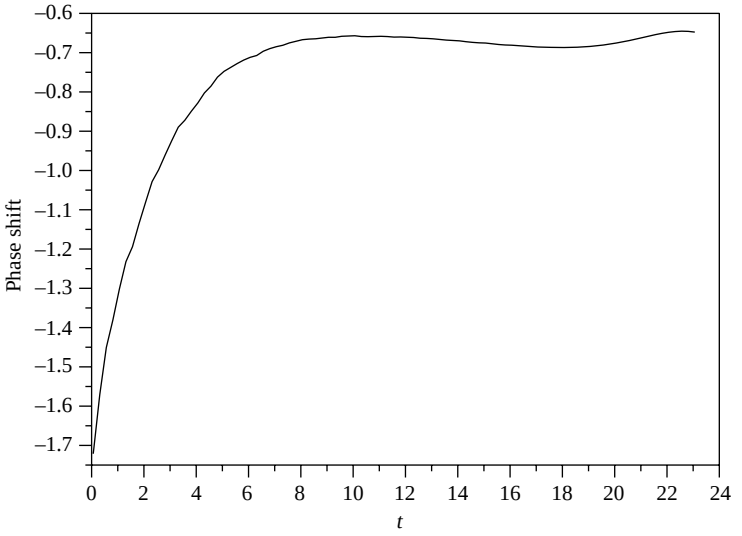

FIGURE 9. Phase shift between h_1 and h_2 as a function of time.

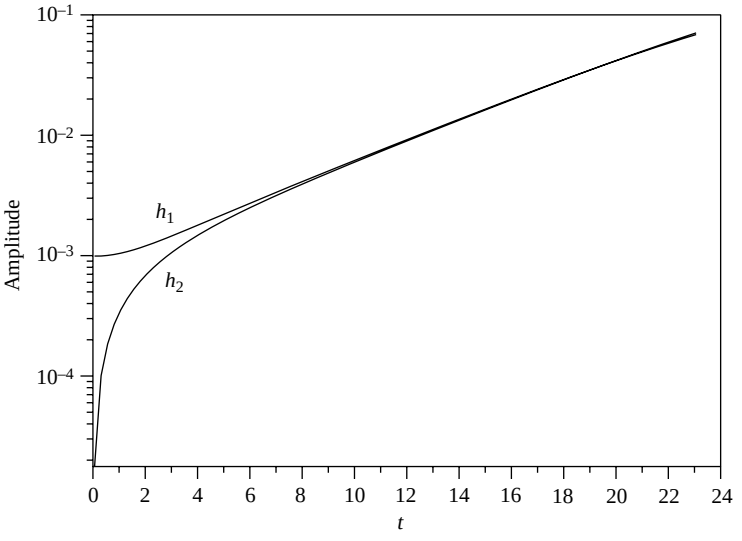

FIGURE 10. Amplitude of perturbations to h_1 and h_2 as a function of time.

good agreement between the nonlinear simulations and the analysis. After a time of $t = 20$, nonlinear effects set in and the phase shift begins to depart from the linear value. Near the end of the simulation, the interfacial profiles are far from sinusoidal (and at these times, the linear theory incorrectly predicts that the upper and lower interfaces intersect), so the phase shifts predicted by linear and nonlinear theories do not agree.

The amplitude growth of the disturbance, $\exp(\omega_I t)$ in (2.6*b*), is also predicted well by the linear analysis. figure 10 shows the amplitude of the disturbances h_1 and h_2 as a function of time. The amplitude of h_2 starts at zero because we do not disturb h_2 initially. Over the first few periods, we see a transient region where the stable modes decay and the unstable mode grows until it dominates the behaviour. Once the

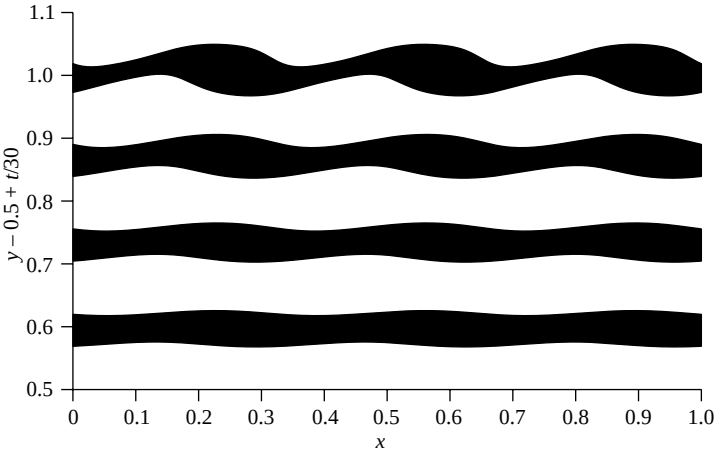

FIGURE 11. Interfacial positions at various times for a high-viscosity middle-layer configuration corresponding for $Re = 0.01$, $N_1 = N_3 = 1$, $N_2 = 5$, $H_1 = 0.475$, $H_2 = 0.525$, $H_3 = 1$, $Ca = 0.001$ and $\theta = \pi/2$.

unstable mode dominates, the amplitudes exponentially grow. If we fit an exponential curve to these plots excluding the first period, we find a growth rate of $\omega_I = 0.193$ for h_1 and $\omega_I = 0.202$ for h_2. There is some spread in the curve fits because, in the initial transient period, the unstable mode does not completely dominate. The exponential growth rate predicted by the linear analysis for the most amplified mode is $\omega_I = 0.204$, thus we again have good agreement with the linear analysis. The linear analysis can be used to predict the amplitudes of the perturbations well, even for conditions under which nonlinear effects are clearly important.

5.2. *More viscous middle layer*

The case of the more viscous middle layer is given by $Re = 0.01$, $N_2 = 5.0$, $H_1 = 0.475$, $H_2 = 0.525$ and $Ca = 0.001$. These are the same conditions as the large-viscosity-ratio case discussed in § 4 (figure 2), except that the Reynolds number is again a factor of 10 smaller. The simulations are done in the same way as for the previous case. The main difference between this case and the previous case is that the most unstable wavelength is approximately 1/3 the layer height instead of 3 times the layer height. Therefore, we use an initial perturbation of non-dimensional wavelength of 1/3 in order to examine the most unstable mode. The computational domain is similar to that shown in figure 5, except the length is set to one and the resolution is increased by a factor of 2. A domain length of three times the wavelength is chosen so that we can determine if there is a nonlinear transfer of energy to wavelengths longer than our initial perturbation. A non-dimensional time step of 1/70 is used for the calculation. The smaller time step is necessary because, although the growth rates of both cases are similar, the oscillation rate for this case is more than 7 times larger.

Figure 11 shows middle-layer profiles in a manner similar to figure 6. In this case, time intervals corresponding to nine periods of propagation are shown. The position of the middle layer is shifted upward with time according the formula, $y = y - 0.5 + t/30$. $t = 0$ again corresponds to having the middle layer centred at $y = 0$, and the middle layer shifts up 0.13 every nine periods. The first profile shown is after about 34 periods of propagation. Again we see a similar behaviour where large beads of fluid separated by thinner strands are formed. The manifestation of nonlinear

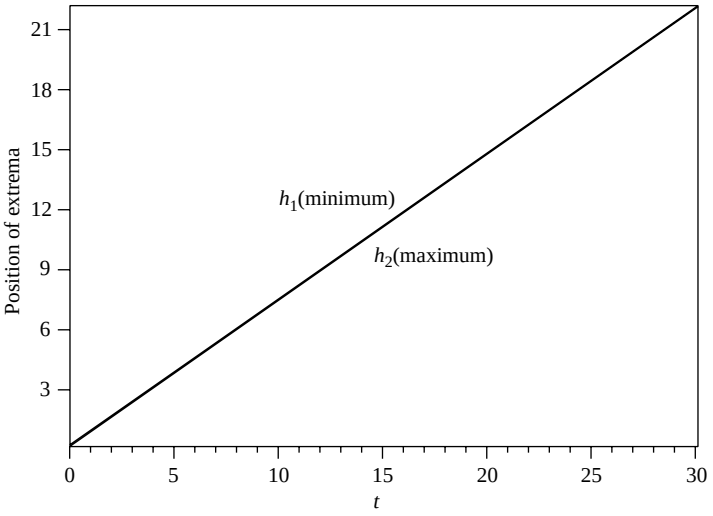

FIGURE 12. Position of minimum of h_1 and maximum of h_2 as a function of time.

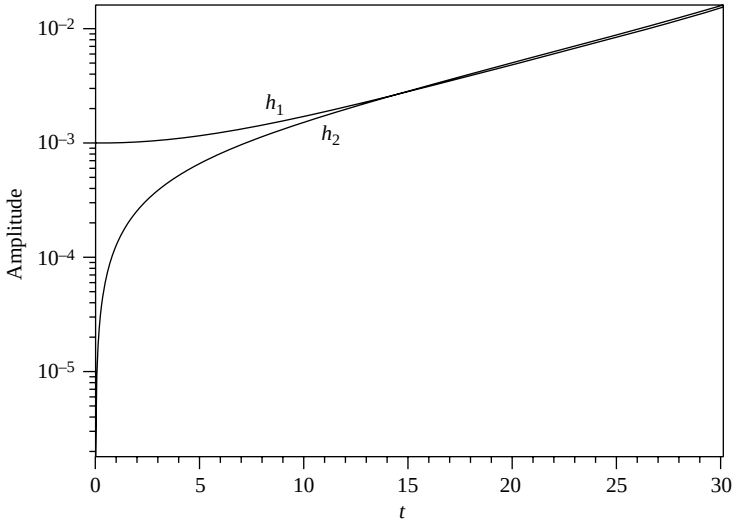

FIGURE 13. Amplitude of perturbations to h_1 and h_2 as a function of time.

effects is thus fairly independent of viscosity ratio and wavelength. In addition, the results remain periodic on a wavelength of $1/3$, which shows that there is no tendency for larger wavelength structures to develop.

As was true in the previous case, the linear analysis gives a very good prediction of the shapes, amplitudes and speeds of the disturbance, even when nonlinear effects should be important. Figures 12 and 13 show the horizontal positions of the perturbation extrema and the perturbation amplitudes as a function of time. The speeds of the disturbances as determined by a linear fit to the curves shown in figure 12 are $c = 0.7288$ for h_1 and $c = 0.7295$ for h_2. In this case, we have excluded the first three periods of propagation. The transient period lasts a greater number of periods because although the growth rates of the disturbances are about the same in both cases, the period of propagation is smaller for this case. The linear analysis predicts

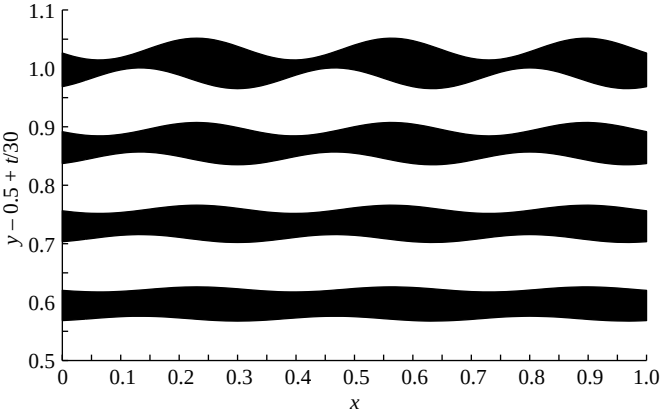

FIGURE 14. Shapes of the interfaces for the most unstable wave predicted from linear theory at the same conditions of figure 11. Parameters for the linear solution are $a_1 = 0.0005$, $\gamma_1 = 0$, $a_2 = 1.05a_1$, $\gamma_2 = -1.82$, $\omega_I = 0.118$ and $c = 0.732$.

a disturbance speed of $c = 0.732$. The exponential growth rates of the disturbances predicted by exponential fits to the curves in figure 13 are $\omega_I = 0.104$ for h_1 and $\omega_I = 0.123$ for h_2. There is some spread due to the initial transient region, which remains significant for longer than 3 periods. The linear analysis predicts a growth rate of $\omega_I = 0.118$.

Figure 14 shows the middle-layer profiles as predicted by the linear analysis in the same manner as figure 11. Because of the large initial transient in the nonlinear simulations of this case, we extrapolated the exponential fits to the curves in figure 13 to $t = 0$ to obtain an initial amplitude rather than picking the same initial amplitude as the simulation. The parameters are then $a_1 = 0.0005$ and $\gamma_1 = 0$ and $a_2 = 1.05a_1$ and $\gamma_2 = -1.82$ in (2.6*b*). Again, we see remarkable agreement between the nonlinear simulations and the analysis even up to perturbation amplitudes that are larger than the middle-layer thickness. This leads us to conclude that the importance of nonlinear effects is better predicted by the ratio of the perturbation amplitude to the domain height than to the middle-layer thickness.

6. Experimental

6.1. *Background*

The experimental configuration used to examine the three-layer inertialess instability in our work employs an industrial curtain coating process (Kistler & Schweizer 1997; Weinstein & Ruschak 2004). Figure 15 shows a schematic of the experimental coating system. A fundamental component of the system is the coating die distributor. The distributor is wide and extends into the plane of figure 15, and serves to transform inlet pipe flows into liquid sheets extending across the die width. The die consists of relatively large cavities and narrow slots running its full width, which partition flow resistance to create relatively widthwise-invariant flow in the slots.

The inclined surface of the coating die, referred to as a slide, allows liquid layers to be stacked on top of one another. As the flow is laminar, the liquid layers remain distinct without mixing. For this experiment, the layers have the same solvent and are thus miscible. As a result, liquid–liquid interfaces do not have an interfacial tension, and interlayer diffusion of mobile components may occur as described in § 6.2. After

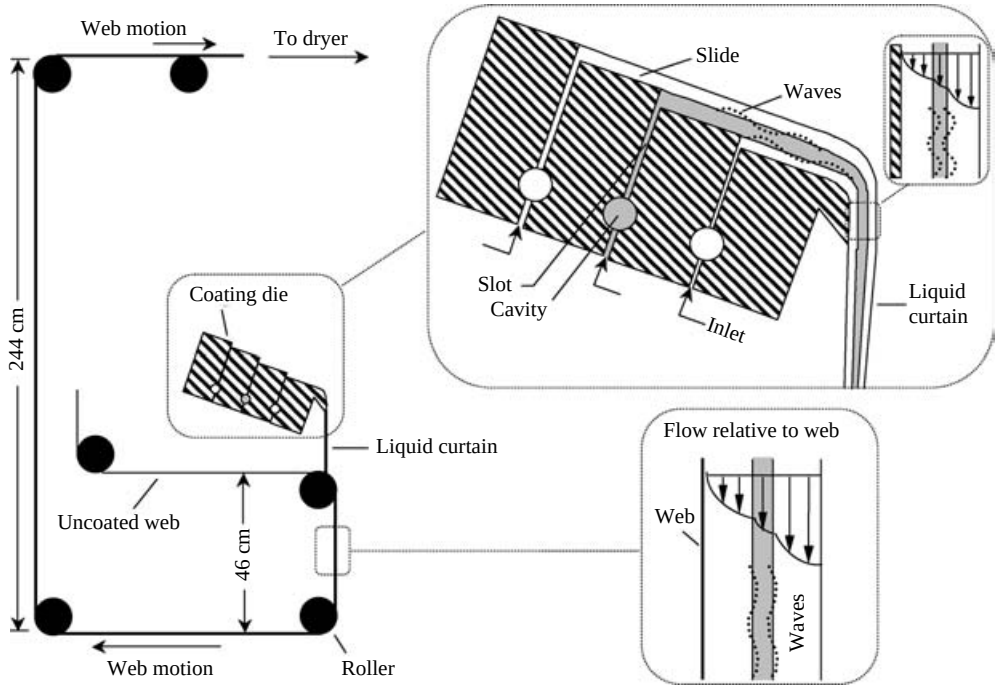

FIGURE 15. Diagram showing portion of coating process. Insets show details of a coating die, including the slide, as well as wave instabilities that may form on the slide and on the web.

stacking up on the slide, the liquid layers fall freely as a layered curtain that is then coated onto a web. The complete multi-layered liquid coating structure is referred to as a coating pack (or pack), which is subsequently dried downstream to create a solid, multiple-layered structure. Typically, each layer of the pack has some functional quality, such as a specific sensitivity to different wavelengths of light in photographic products. In our experiments, however, the layer viscosities are chosen to exhibit a three-layer instability, and non-photoactive optical density material is placed in the coating to allow interfacial instabilities to be observed, as will be discussed in § 6.3.

The study of three-layer flow along a stationary wall using the system in figure 15 is complicated by the fact that wave instabilities can occur on both the slide and the web (Weinstein 1990; Kistler & Schweizer 1997). Despite the fact that the web is moving, a shift in frame of reference to that translating with the web recovers gravity-driven flow along a stationary wall. As will be shown in what follows, it is the flow along the web, and not the slide, that is typically suitable for studying the low-Reynolds-number regime.

On a web moving at speed V, the gravity-driven flow is small enough that the total liquid-film thickness, H_3^*, may be approximated as if all layers are in plug flow, i.e. $H_3^* = q/V$, where q is the cumulative volumetric flow rate per unit width delivered from the die to all layers. A typical web velocity is of the order of a few hundred centimetres per second and q is typically $2\,\mathrm{cm^2\,s^{-1}}$. This gives a wet-film thickness (i.e. prior to drying) of the order of 100 μm. The volumetric flow per unit width induced by gravity in the web frame is $q_w \sim U_s H_3^*$, where U_s is given in (2.1*a*). For a 1 poise liquid having a density of $1\,\mathrm{g\,cm^{-3}}$ and a 100 μm coating on a vertical web path ($\theta = 90°$), this estimate gives a volumetric flow per unit width in the web frame of $4.9 \times 10^{-4}\,\mathrm{cm^2\,s^{-1}}$; the corresponding Reynolds number in (2.1*b*) has the same numerical value. Thus, the

Reynolds number in the web frame is exceedingly small, and an essentially inertialess three-layer flow may be achieved. Note that in this example, the average velocity of the film in the web frame, i.e. q_w/H_3^*, is 3.3×10^{-2} cm s^{-1}. This is negligible compared with typical web speeds and justifies our contention that the film thickness of each layer may be calculated as if the flow is a plug on the web.

On the slide, the individual thicknesses of the liquid layers are not linearly proportional to the volumetric flow rate delivered to each layer. A good approximation to the total thickness of the liquid layers, H_3^*, is given as:

$$H_3^* \approx \left(\frac{3q\mu_1}{\rho g \sin\theta} \right)^{1/3}, \tag{6.1}$$

where again, q is the cumulative volumetric flow rate per unit width of all layers. The approximation (6.1) is supported by theoretical predictions from Weinstein (1990) for Newtonian liquids. In the above example of a 100 μm coated film on the web, the corresponding film thickness on the slide is approximately 1.5 mm according to (6.1) which is of the order of ten times thicker. Note that according to (6.1) and (2.1*a*), $U_s H_3^* = 3q/2$, and thus the Reynolds number in (2.1*b*) may be expressed as $Re = 3\rho q/2\mu_1$. For the typical coating conditions given in the previous paragraph, this Reynolds number is $O(1)$. Thus, only the flow on the web can be used to examine low-Reynolds-number instabilities.

6.2. *Water diffusion*

Arguments in § 6.1 suggest that the low-Reynolds-number three-layer instability can be studied experimentally by examining the flow on the web. Unfortunately, these experiments are complicated by the fact that wave instabilities, having appreciable inertia, may still arise on the slide (see § 6.1). We have indeed found this to be the case – coating packs exhibiting large growth on the web are often prone to slide wave instabilities. The inertia in the slide flows allows appreciable wave growth, even for two-layer systems. Although slide instabilities typically have wavelengths of the order of a factor of 10 larger than inertialess instabilities arising on the web, they are often extreme enough to affect locally the total pack thickness, H_3^*, coated on the web. This, in turn, can affect the growth rate on the web and make it difficult to assess the inherent stability of the coating structure at its mean thickness.

We have discovered a way to avoid these slide waves and, in the process, have elucidated an important physical mechanism present in coating flows having multiple layers. In particular, we have found that diffusion of water between layers, driven by composition differences, may substantially alter the liquid viscosities on the web after the pack is coated, such that inertialess instabilities arise, but slide instabilities are avoided. In simple solutions consisting of primarily gelatin and water, we have evidence that differences in the gelatin weight percentage (gel %) between layers drive water diffusion, where water migrates from low gel % to high gel %. For a given diffusion coefficient, D, and length scale, L, a diffusion time can be estimated as

$$t^* \sim \frac{L^2}{4D}. \tag{6.2}$$

The diffusion coefficient of water in gelatin is approximately 3×10^{-6} cm^2 s^{-1} (Gehrmann & Kast 1978). Inertialess instabilities are accentuated with a thin middle layer. For a thin layer of 7 μm wet thickness, the time necessary for the water to diffuse through this layer is, using (6.2), approximately 0.04 s. This is short compared with the typical time available for wave growth on the inclined web path used in our

experiments. Note that for a 150 μm coating structure, however, the time required for the diffusion front to pass through all layers is about 19 s. Thus, a thin layer can completely change its water composition and associated viscosity quickly in the time available on the inclined web path, even as the whole coating structure continues to evolve through diffusion.

Water diffusion also occurs on the slide where the liquid layers first come in contact. However, the layer thicknesses on the slide are much larger than the diffusion length scale for water. As a result, although there is some blurring of interfaces on the slide surface, our experimental results indicate that the layer viscosities do not change enough to cause significant wave instabilities on the slide.

In order for a three-layer inertialess instability to arise on an inclined web, water diffusion must drive the layers into a configuration having a viscosity difference across a thin middle layer. In particular, the viscosity of the thin middle layer must be either lower or higher than that of both the top and bottom layers, as described by Weinstein & Chen (1999) and in previous sections. We restrict attention to symmetrical coating packs in which the layer composition and thickness of the top and bottom layers are identical. To avoid slide instabilities, we would like the layers to be nominally matched in viscosity on the slide. Therefore, in our experiments, we deliver the same initial viscosity in each layer to the coating die but different gel % by weight. This is accomplished by using viscosifying agents (thickeners), which have the property that small additions cause large changes in viscosity. As the starting gel % in the layer is varied, the amount of polymeric thickener is adjusted to achieve the same initial viscosity in each layer. Given enough time, and assuming that the water diffusion process is driven solely by the gel %, each layer in the coating pack equilibrates to the same gel %. We further assume that the mass of gelatin and thickener initially delivered to any given layer remains the same throughout the diffusion process. At equilibrium, then, the viscosity attained in each layer is different, given that the thickener concentration is different.

Figure 16 shows how water is anticipated to diffuse in such experimental packs for two different gel % configurations. In a case where there is a high gel % middle layer and low gel % adjacent layers (with all layers initially having the same viscosity), water diffuses into the middle layer, causing a low-viscosity middle-layer configuration (see figure 16*a*). Similarly, for a gel % configuration in which there is a low gel % middle layer and high gel % adjacent layers, water diffuses out of the middle layer, leaving a high-viscosity middle-layer configuration (see figure 16*b*).

Although not strictly valid, the equilibrium value of the gel % in each layer gives us a rough measure of the viscosity attained in the diffusing symmetrical pack. Because the middle layer is thin compared with the top and bottom layers, the equilibrium gel % of each layer in the coating pack is very close to that of the top and bottom layers. The associated viscosities in the top and bottom layers, then, are approximately equal to the starting values prior to diffusion. The viscosity of the middle layer, μ_2, can change significantly and may be expressed in terms of the equilibrium gel %, X, via an empirical quadratic equation as

$$\mu_2 = aX^2 + bX + c. \tag{6.3a}$$

In (6.3*a*), the quantities a, b and c are constants that depend on the layer composition (see § 6.3).

Because of water diffusion, the thicknesses of the layers also change. The equilibrium thickness of each layer may be calculated by assuming that the liquid layer densities are approximately equal (see § 6.3 for justification) and remain constant throughout

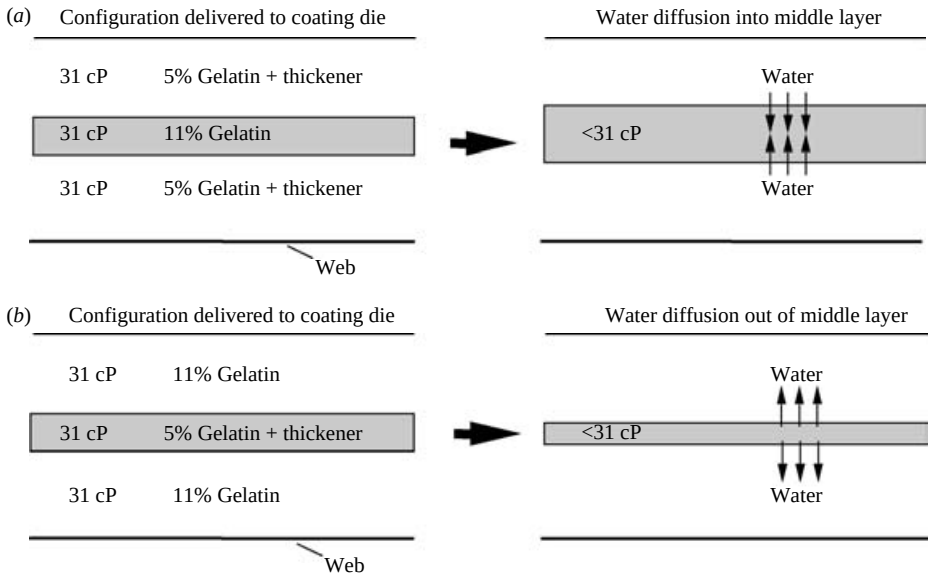

FIGURE 16. Diagram showing how the layer viscosities and thicknesses of a coating pack can change as a result of water diffusion, starting from a configuration where layers initially have the same viscosity. (*a*) A high gel % middle layer is sandwiched between two lower gel % layers. Water diffusion drives water into the middle layer, and its viscosity drops while its thickness increases. (*b*) A low gel % middle layer is sandwiched between two higher gel % layers. Water diffusion drives water out of the middle layer, and its viscosity increases while its thickness decreases.

the diffusion process. The equilibrium thickness of the middle layer, D_2^* is calculated assuming that only water moves between the layers as:

$$D_2^* = \frac{D_2^0 x_2}{X}, \tag{6.3b}$$

where D_2^0 and x_2 are the starting thickness and gel % of the middle layer, respectively. The equilibrium thickness of the top and bottom layers, D_1^* and D_3^*, follow as:

$$D_1^* = D_3^* = H_3^* - \tfrac{1}{2} D_2^* \tag{6.3c}$$

where H_3^* is the pack thickness that is constant throughout the diffusion process, according to our constant-density assumption. Note that according to the formulation in § 2:

$$H_k^* = \sum_{j=1}^{k} D_j^* \text{ for } k \in [1, 3]. \tag{6.3d}$$

In the theoretical analysis and simulations of this paper, we have assumed that the viscosity of each layer is constant throughout the wave growth process. According to the discussion above, there is a gel % profile across the coating thickness that evolves, even as waves grow. Thus, the viscosity will vary across the coating thickness. Nevertheless, we propose that it is the viscosity jump across the interface that is the predominant source of instability – even in these diffusing systems. We will use the equilibrium values of the viscosity and layer thicknesses as given by (6.3) in the model for qualitative comparisons with experiment.

6.3. *Experimental design*

As stated previously, we restricted attention to symmetrical three-layer coating structures in our experiments. We chose a wet coating thickness of the top and bottom layers to be 71 μm and a 7 μm coating thickness in the middle layer, and the width of all coatings was 4 in. Bone gelatin with an isoelectric point of 4.9 (Rose 1978) was used in all experiments. The gelatin weight% of the bottom and top layers of the coating pack were examined in the range of 5 %–11 % by weight in 1 % increments. The viscosity of each layer was maintained at nominally 31 cP through the use of a thickener; the thickener used was a potassium salt of octadecyl hydroquinone sulfonate. In the 5 %–11 % gel range, the densities of the liquid layers were essentially constant, varying only from 1.01 to 1.03 g cm^{-3}; this justifies the constant-density assumption used in the derivation of (6.6*b*). The top and bottom layers also had TRITON X-200E surfactant (a sodium salt of octylphenoxydiethoxyethane sulfonate, Union Carbide) solution added at 2.6 % by weight. This surfactant provided protection from Marangoni flows induced by contamination that could lead to holes in the curtain, and it ensured that the top and bottom layers fully wetted the middle layer in the curtain. The equilibrium surface tension of the top and bottom surfaces was 30 dyn cm^{-1}. The middle layer contained a black carbon slurry such that its optical density on the web was about 1, and the layer also had a nominal viscosity of 31 cP.

The middle layer had two possible compositions. In the first configuration, the middle layer consisted of 11 % gelatin by weight and, in the second configuration, the middle layer consisted of 5 % gelatin by weight plus thickener. For the 11 % middle layer, empirical coefficients of the viscosity curve (6.6*a*) were determined by simple dilution of the liquid to be $a = 0.55$, $b = -4.22$, and $c = 11.44$. For the 5 % middle layer, we generated a concentrated version of the liquid having the appropriate amount of thickener, such that when it was diluted to 5 %, it achieved the desired viscosity of 31 cP. In this way, the viscosity curve (6.6*a*) could be generated through dilution; the empirical coefficients obtained were $a = 1.72$, $b = -8.02$, and $c = 28.11$. Note that both empirical fits are only valid in the range of 5 % to 11 % gel.

Our experimental curtain coating system (figure 15) has an appreciable vertical web path after coating, consisting of a 46 cm drop followed by a 244 cm rise. The direction of the web motion with respect to gravity does not affect the observed wave phenomena, as it may be viewed as occurring in the web frame of reference (§ 6.1); the cumulative web path length relevant to wave instabilities, L, is thus 209 cm. The horizontal web section adjoining the two vertical sections does not impact the wave growth (except through the added short time available for water diffusion on this section), as there is no gravity-driven flow here. All coatings were made at a web speed, V, of 152.4 cm s^{-1} on 7 mil polyethylene terephthalate (PET) web. The effective time for wave growth was $t^* = L/V = 1.9$ s. All three layers of coating liquid contained gelatin, therefore, they were delivered at 40 °C to prevent setting in the pumps and delivery lines, and an enclosure around the entire web path was nominally maintained at this temperature. Downstream of the inclined web path, the coating was chilled to immobilize it and, subsequently, was dried. All data provided in this paper are based on dried coatings on the PET web.

6.4. *Results*

Table 2 provides post-diffusion equilibrium values of the viscosity and thickness for each layer of the coating structure using (6.3) and following the discussion in § 6.2. In addition, table 2 contains the theoretical dimensional growth rate, $\omega_I^* = \omega_I U_s / H_3^*$, and wavelength, $\lambda^* = H_3^* \lambda$, associated with the wave having largest growth over all

Case	Gel % bottom/top	Viscosity (cP)		Thickness (μm)		Max growth wave	
		Bottom/top	Middle	Bottom/top	Middle	λ^* (mm)	ω_I^* (s^{-1})
(*a*) A	5	31	4.0	66.8	15.4	0.74	4.92
B	6	31	5.7	68.1	12.8	0.59	4.85
C	7	31	8.6	69.0	11.0	0.52	4.03
D	8	31	12.6	69.7	9.6	0.49	3.04
E	9	31	17.6	70.1	8.6	0.49	2.05
F	10	31	23.8	70.7	7.7	0.55	0.98
G	11	31	31.0	71.0	7.0	—	—
(*b*) A′	5	31	31.0	71.0	7.0	—	—
B′	6	31	41.9	71.6	5.8	0.36	0.023
C′	7	31	56.2	72.0	5.0	0.36	0.029
D′	8	31	74.0	72.3	4.4	0.078	0.83
E′	9	31	95.2	72.6	3.9	0.042	1.96
F′	10	31	119.9	72.8	3.5	0.030	2.55
G′	11	31	148.0	72.9	3.2	0.026	2.81

TABLE 2. Approximate diffused pack structures at equilibrium with growth results. (*a*) Middle layer 11 % gel; (*b*) 5 % gel.

wavelengths for each diffused pack structure from inertialess theory. In an experiment in which noise excites waves at all wavelengths and given enough time, it is this wave that will be predominantly observed in the coating. As shown in table 2, when the growth rate is large, the wavelengths associated with cases of a high-viscosity middle-layer (i.e. the middle layer starts at 5 % gel) are of the order of 10 times smaller than those having a low-viscosity middle layer (i.e. the middle layer starts at 11 % gel). Predicted wavelengths for the low-viscosity middle layer configurations in table 2 lie in the range of 0.49–0.74 mm, while those for a high-viscosity middle layer lie in the range of 0.026–0.078 mm. Note that there is anomalous wave growth data (much longer wavelength and lower growth) for cases B′ and C′ in table 2. These results arise because the viscosity jump across the interface is not large enough to induce the nearly complex conjugate frequency modes required for large growth, as described at the beginning of § 4. The maximum growth rates and wavelengths for these cases are of the same order as those found in a two-layer inertialess system (Loewenherz & Lawrence 1989; Chen 1993) and cannot be observed in our experiments in the time available for wave growth. Note also that no wave data is supplied in table 2 for cases G and A′, as these are single-layer systems that do not exhibit wave growth.

Figure 17 shows typical images of coating samples having a post-diffusion low-viscosity middle layer (figure 17*a*) and high-viscosity middle layer (figure 17*b*). Because optical density is found in the middle layer, darker and lighter regions of the images indicate a thickening and thinning of the layer, respectively. Figures 17(*a*) and 17(*b*) give images corresponding to cases A (low-viscosity, middle layer) and G′ (high-viscosity, middle layer), respectively, for a 3 mm length of coating. The images in figure 17 have wavelengths that are of the order of those predicted in table 2, and clearly show the theoretically anticipated difference in wavelength predicted by the linear model. This is despite the fact that there is a three-dimensional character to the waves across the coating width in figure 17 (waves in the linear model are assumed to be two-dimensional). While the origin of this three-dimensional character is not known, it is possible that they may be triggered by small inhomogeneities in the liquid or by local viscosity variations incurred during diffusion.

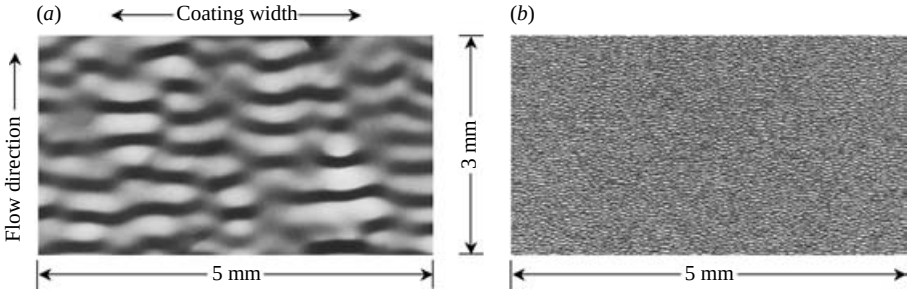

FIGURE 17. Typical comparison between coating samples having a post-diffusion low-viscosity middle-layer and high-viscosity middle-layer configuration. (*a*) A sample having a low-viscosity middle-layer configuration corresponding to case A in table 2. (*b*) A sample having a high-viscosity middle-layer configuration corresponding to case G′ in table 2.

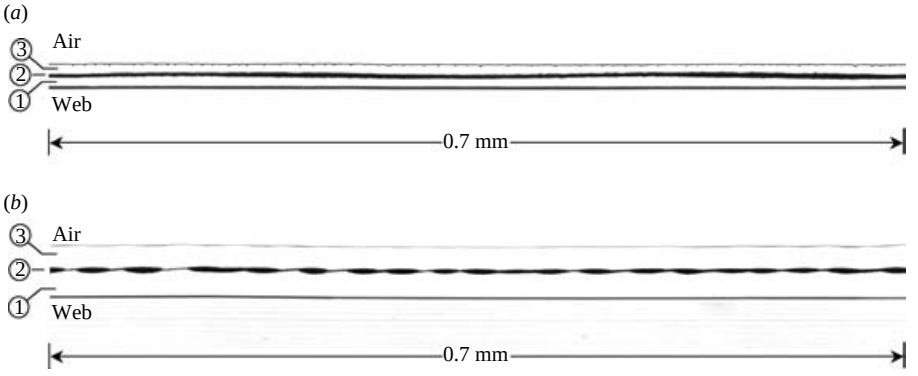

FIGURE 18. Cross-sections of typical post-diffusion low- and high-viscosity middle-layer samples corresponding to top views shown in figure 17. (*a*) Case A in table 2, having a low viscosity middle-layer; (*b*) case G′ in table 2, having a high-viscosity middle layer. The cross-sections are taken in the flow direction and are perpendicular to the images shown in figure 17.

Figure 18 provides cross-sectional views of a 0.7 mm section of the coating samples shown in figure 17; the cross-sections are taken in the flow direction (the gravity-driven flow moves from left to right in the figures) and perpendicular to the plane of the coating images in figure 17. The superimposed numbers denote the individual layers, where layer 1 is the bottom and layer 3 is the top; recall that the middle layer 2 contains the optical density. The cross-sections are taken after the dried gelatin coatings have been swelled by water to enhance resolution. Note that although the coated thicknesses of both samples in figure 18 were the same, their swelled layer thicknesses are different owing to the different amount of total gelatin in both structures. Additionally, the swelled layer thicknesses are different from those on the inclined web path after coating and, so, the cross-sections can provide only a qualitative picture of the actual wave phenomenon. Nevertheless, the cross-sections clearly show that the middle layer exhibits a varicose wave pattern (i.e. there is a thinning and thickening of the layer) in figures 18(*a*) and 18(*b*). Figure 18(*a*) also shows that there is a sinuous component (i.e. the two interfaces have a tendency to move in phase) of the waveform superimposed on these thickness variations. This sinuous component may also be observed in figure 18(*b*), although to a lesser extent.

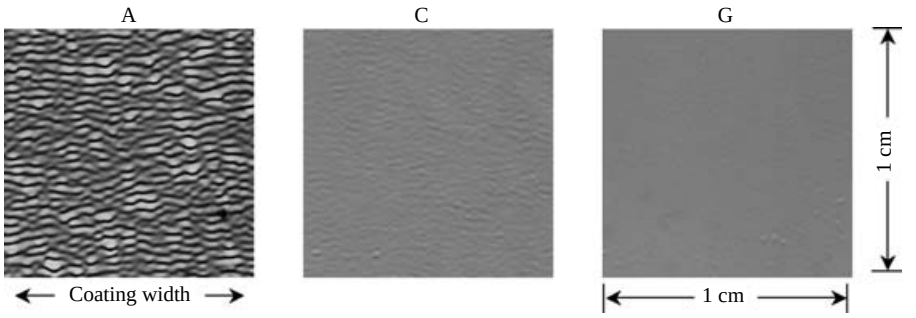

FIGURE 19. Coating samples for a post-diffusion low-viscosity middle-layer pack configuration corresponding to conditions A, C, and G in table 2. As the difference in the gel % between the middle and top and bottom layers decreases, the severity of the wave imperfection decreases.

Note that the top interface (between layer 3 and air, which corresponds to the free surface when the film is in its liquid state) appears to be nominally flat in both cross-sections in figure 18 to within the resolution of the cross-sectioning technique and in agreement with numerical simulations.

The cross-section in figure 18(*a*) (corresponding to case A in table 2) is in strong qualitative agreement with either of the first two middle-layer profiles of the nonlinear simulation shown in figure 6. Figure 18(*a*) also agrees well with the interface shapes constructed from linear theory in figure 7. Similarly, the cross-section in figure 18(*b*) (corresponding to case G′ in table 2) agrees well with the last profile of figure 11, revealing thin ascending strands alternating with large beads of fluid.

The images in figure 18 show large thickness variations in the internal layer that violate the linearity assumption implicit in the theoretical data of table 2. The apparent nonlinearity of the waveforms, which also manifests itself in the non-uniform wavefronts along the coating width in figure 17, precludes a strictly valid comparison of our theoretical wavelengths in table 2 with those in the images. Nevertheless, a simple division of the length of the coating samples in figures 17 and 18, by the number of wave amplitudes (the dark peaks), gives an approximate wavelength of about 0.4 for case A and 0.04 for case G′. Considering the approximate nature of our diffusion model, and the nonlinear effects, these values are reasonably close to those given in table 2. Additionally, note that for a time of 1.9 s on the vertical web path and values of ω_I^* from table 2, wave growth, according to (6.1) for cases A and G′ are 1.15×10^4 and 2.08×10^2, respectively. These large growths are at least consistent with the occurrence of the observed nonlinear waveform, because even small disturbances are being magnified greatly.

Figures 19 and 20 give magnified top view images of coating samples corresponding to the post-diffusion low-viscosity and high-viscosity middle layers, respectively, for selected conditions shown in table 2. Direct comparison between the two figures may be made by noting that the primed and unprimed cases (A and A′, G and G′) correspond to the same initial top- and bottom-layer properties, and only the middle layer is different. In figure 19, which has an 11 % gel middle layer, case A shows the greatest severity, while in figure 20, which has a 5 % gel middle layer, case A′ shows no waves. Case G in figure 19 shows no waves, but case G′ in figure 20 shows the greatest severity waves. Intermediate coating samples between the cases shown in figures 19 and 20, not shown here, continue the trends shown in these figures. That is, the data in both figures indicate that as the gel % difference between the middle and

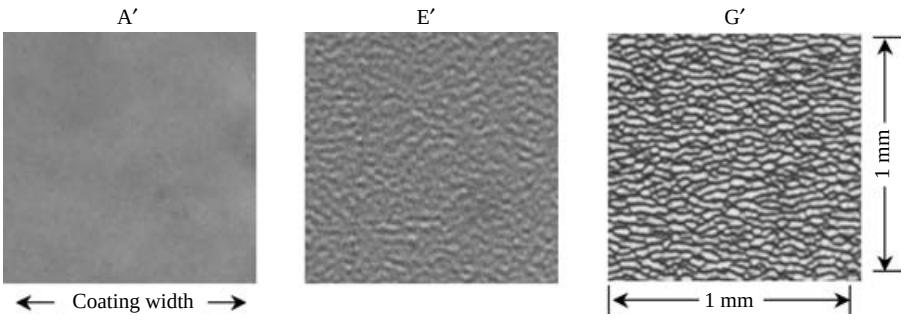

FIGURE 20. Coating samples for a post-diffusion high-viscosity middle-layer pack configuration corresponding to conditions A′, E′ and G′ in table 2. As the difference in the gel % between the middle and top and bottom layers increases, the severity of the wave imperfection increases.

adjacent layers decreases, the severity of the waves decreases in qualitative agreement with the growth data in table 2.

7. Summary and closing comments

We have provided a rare example, if not the first, of the crucial role of the Reynolds stress in the mechanism of instability at small Reynolds numbers. The vestige of the Reynolds stress remains, even in the limit of $Re \to 0$. The origin of the small-Reynolds-number instability in a two-layer liquid film falling along a flat plate was found to be due to the interfacial shear work, even in the limit of $Re \to 0$ (Jiang *et al.* 2004). Three-layer film flows exhibit much larger magnitude instabilities when the middle layer is relatively thin and has a much larger or smaller viscosity compared with its adjacent layers (Weinstein & Chen 1999). Although the magnitudes of the interfacial shear and viscous dissipation terms remain much larger than other terms in the energy budget, the viscous dissipation is slightly greater than the destabilizing effect of interfacial shear, even in the limit of $Re \to 0$. Therefore, unlike the two-layer case, Reynolds stresses in the low viscosity layers are found to be an essential agent of instability. The mechanism of the instability for finite but small Reynolds number has been shown to remain the same, even as $Re \to 0$. Thus, the notion of an inertialess instability is clearly established and conclusions drawn from previous work are validated.

The notion of inertialess instability has been supported further by experiments and numerical simulation. The simulations show that regardless of whether the middle layer is more or less viscous than the other layers, nonlinear effects manifest themselves by forming large beads of middle-layer fluid connected by thin strands. Although nonlinear effects strongly affect the evolution of the shape of the layers, the linear analysis does an excellent job of predicting the amplitude growth and propagation velocity well after nonlinear effects become significant. This is also observed in experiments.

The linear theories and nonlinear simulation presented here do not include effects of water diffusion. Yet, even in the presence of water diffusion, predictions are in good agreement with experimental observations. This supports our proposed mechanism regarding the direction of water diffusion as dictated by the gel % differences across the layers. It also supports our contention that the viscosity differences across the interfaces are predominantly responsible for the instability, even when layer viscosities

vary internally. The factor of 10 difference in wavelength between the post-diffusion low- and high-viscosity middle-layer configurations allows us easily to distinguish experimentally the direction of water diffusion in the coating structure. For a low- or high-viscosity middle-layer configuration, table 2 shows there is a relative insensitivity of the wavelength to changes in pack structure. This partially accounts for our comparisons between theory and experiment being successful, despite the relatively simple approximations used to determine pack structures upon which wave predictions are made.

More sophisticated diffusion predictions could be directly coupled with a hydrodynamic theory for wave growth that allows viscosity to vary in each layer to obtain a more quantitative comparison with experiments. This coupled theory, of course, would be predicated on the fact that we can characterize the diffusion process occurring accurately. Such a coupled analysis is a subject for future work.

We would like to thank Lola Darmon and Paul Devries of the Eastman Kodak Company for providing the respective cross-sections and pictures of the coating samples. We would also like to thank the Eastman Kodak Company for providing the time and facilities to perform the experimental work. S. P. L. and W. Y. J. acknowledge the NSF support Grant CTS-0138057. W. Y. J. is also partially supported by the NASA Solid Earth and Natural Hazard Program.

REFERENCES

Benjamin, T. B. 1957 Wave formation in laminar flow down an inclined plane. *J. Fluid Mech.* **2**, 554–574.

Chen, K. P. 1993 Wave formation in gravity-driven low Reynolds number of two liquid films down an incline plane. *Phys. Fluids* **5**, 3038–3048.

Chen, K. P. 1995 Interfacial instability in stratified shear flows involving multiple viscous and viscoelastic fluids. *Appl. Mech. Rev.* **48**, 763–776.

Gehrmann, D. & Kast, W. 1978 Drying of gels. In *Proc. First Intl Symp on Drying* (ed. A. S. Mujumdar), pp. 239–246. Science Press, Princeton.

Helenbrook, B. T. 2001 A two-fluid spectral element method. *Comput. Meth. Appl. Mech. Engng* **191**, 273.

Helenbrook, B. T. & Baker, T. J. 2002 An adaptive spectral element method for two-fluid flows. FEDSM2002-31227. In *Proc. of the 2002 Joint ASME/European Fluids Engng Division Summer Conf. Montreal, Canada.*

Hooper, A. P. 1985 Long-wave instability at the interface between two viscous fluids: thin layer effects. *Phys. Fluids* **28**, 1613–1618.

Hooper, A. P. & Boyd, W. G. 1983 Shear flow instability at the interface between two viscous fluid. *J. Fluid Mech.* **128**, 507–528.

Hooper, A. P. & Grimshaw, R. 1985 Nonlinear instability at the interface between two viscous fluids. *Phys. Fluids* **28**, 37–45.

Jiang, W. Y., Helenbrook, B. & Lin, S. P. 2004 Inertialess instability of a two layered liquid film flow. *Phys. Fluids* **16**, 652–663.

Joseph, D. D. & Renardy, Y. Y. 1992 *Fundamentals of Two Fluids Dynamics*. Springer.

Kao, T. W. 1968 Role of viscosity stratification in the instability of two-layer flow down an incline. *J. Fluid Mech.* **33**, 561–572.

Kistler, S. F. & Schweizer, P. M. 1997 *Liquid Film Coating*. Chapman & Hall.

Kliakhandler, I. L. 1999 Long interfacial waves in multiplayer thin films and coupled Kuramoto–Sivashinsky equations. *J. Fluid Mech.* **391**, 45–65.

Kliakhandler, I. L. & Sivashinsky, G. I. 1997 Viscous damping and instabilities in stratified liquid film flowing down a slightly inclined plane. *Phys. Fluids* **9**, 23–30.

Li, C. H. 1969 Instability of three-layer viscous stratified flow. *Phys. Fluids* **12**, 2473–2481.

Loewenherz, D. S. & Lawrence, C. J. 1989 The effect of viscosity stratification on the instability of a free surface flow at low Reynolds number. *Phys. Fluids* **1**, 1686–1693.

Renardy, Y. 1985 Instability at the interface between two shearing fluids in a channel. *Phys. Fluids* **28**, 3441–3443.

Renardy, Y. 1987 The thin-layer effect and interfacial stability in two-layer Couette flow with similar liquid. *Phys. Fluids* **30**, 1627–1637.

Rose, P. I. 1978 Gelatin. In *The Theory of the Photographic Process*, 4th edn (ed. T. H. James), pp. 51–67. Macmillan.

Tilley, B. S., Davis, S. H. & Bankoff, S. G. 1994*a* Linear stability theory of two-layer fluid flow in an inclined channel. *Phys. Fluids* **6**, 3906–3922.

Tilley, B. S., Davis, S. H. & Bankoff, S. G. 1994*b* Nonlinear long-wave stability of superposed fluids in an inclined channel. *J. Fluid Mech.* **277**, 55–83.

Wang, C. K., Seaborg, J. J. & Lin, S. P. 1978 Instability of multilayered liquid film. *Phys. Fluids* **21**, 1669–1673.

Weinstein, S. J. 1990 Wave propagation in the flow of shear-thinning fluids down an incline. *AIChE J.* **36**, 1873–1889.

Weinstein, S. J. & Chen, K. P. 1999 Large growth rate instabilities in three-layer flow down an incline in the limit of zero Reynolds number. *Phys. Fluids* **11**, 3270–3282.

Weinstein, S. J. & Kurz, M. R. 1991 Long-wavelength instabilities in three-layer flow down an incline. *Phys. Fluids* **3**, 2680–2687.

Weinstein, S. J. & Ruschak, K. J. 2004 Coating flows. *Annu. Rev. Fluid. Mech.* **36**, 29–53.

Williams, R., Burrage, K., Cameron, I. & Kerr, M. 2002 A four-stage index 2 diagonally implicit Runge–Kutta method. *Appl. Num. Maths* **40**, 415–432.

Yih, C. S. 1963 Stability of liquid flow down an inclined plane. *Phys. Fluids* **6**, 321–334.

Yih, C. S. 1967 Instability due to viscosity stratification. *J. Fluid Mech.* **27**, 337–352.